ISSN 1674-1056
http://cpb.iphy.ac.cn
http://iopscience.iop.org/cpb
中国物理 B
Chinese Physics
中国物理 Chinese Physics B

Momentum-space crystal in narrow-line cooling of ^{87}Sr

Jian-Xin Han(韩建新), Ben-Quan Lu(卢本全), Mo-Juan Yin(尹默娟), Ye-Bing Wang(王叶兵), Qin-Fang Xu(徐琴芳), Xiao-Tong Lu(卢晓同), Hong Chang(常宏)

Citation: Chin. Phys. B . 2019, 28(1): 013701. **doi:** 10.1088/1674-1056/28/1/013701
Journal homepage: http://cpb.iphy.ac.cn; http://iopscience.iop.org/cpb

What follows is a list of articles you may be interested in

Strontium optical lattice clock at the National Time Service Center

Ye-Bing Wang(王叶兵), Mo-Juan Yin(尹默娟), Jie Ren(任洁), Qin-Fang Xu(徐琴芳), Ben-Quan Lu(卢本全), Jian-Xin Han(韩建新), Yang Guo(郭阳), Hong Chang(常宏)

Chin. Phys. B . 2018, 27(2): 023701. **doi:** 10.1088/1674-1056/27/2/023701

Deterministic loading of an individual atom:Towards scalable implementation of multi-qubit

Jun He(何军), Bei Liu(刘贝), Jie-Ying Wang(王杰英), Wen-Ting Diao(刁文婷), Gang Jin(靳刚), Jun-Min Wang(王军民)

Chin. Phys. B . 2017, 26(11): 113702. **doi:** 10.1088/1674-1056/26/11/113702

Fractal dynamics in the ionization of helium Rydberg atoms

Xiulan Xu(徐秀兰), Yanhui Zhang(张延惠), Xiangji Cai(蔡祥吉), Guopeng Zhao(赵国鹏), Lisha Kang(康丽莎)

Chin. Phys. B . 2016, 25(11): 110301. **doi:** 10.1088/1674-1056/25/11/110301

Improving the intensity and efficiency of compressed echo in rare-earth-ion-doped crystal

Xiu-Rong Ma(马秀荣), Yu-Qing Liang(梁裕卿), Song Wang(王松), Shuang-Gen Zhang(张双根), Yun-Long Shan(单云龙)

Chin. Phys. B . 2016, 25(7): 070302. **doi:** 10.1088/1674-1056/25/7/070302

Photoassociation of ultracold RbCs molecules into the (2)0$^-$ state (v=189,190) below the $5S_{1/2}$+$6P_{1/2}$dissociation limit

Chang Xue-Fang, Ji Zhong-Hua, Yuan Jin-Peng, Zhao Yan-Ting, Yang Yong-Gang, Xiao Lian-Tuan, Jia Suo-Tang

Chin. Phys. B . 2013, 22(9): 093701. **doi:** 10.1088/1674-1056/22/9/093701

Momentum-space crystal in narrow-line cooling of ^{87}Sr*

Jian-Xin Han(韩建新)[1,2], Ben-Quan Lu(卢本全)[1], Mo-Juan Yin(尹默娟)[1], Ye-Bing Wang(王叶兵)[1,2], Qin-Fang Xu(徐琴芳)[1], Xiao-Tong Lu(卢晓同)[1,2], and Hong Chang(常宏)[1,2,†]

[1] *Key Laboratory of Time and Frequency Primary Standards, National Time Service Center, Chinese Academy of Sciences, Xi'an* 710600, *China*
[2] *University of Chinese Academy of Sciences, Beijing* 100049, *China*

(Received 12 August 2018; revised manuscript received 30 October 2018; published online 12 December 2018)

The discovery of the momentum space crystal based on the alkaline-earth atom ^{88}Sr in narrow-line cooling has paved the way to explore this novel physical phenomenon in other cold atom systems. In this paper, a momentum space crystal based on the fermions ^{87}Sr in narrow-line cooling of transition $^1S_0$–$^3P_1$ is demonstrated. We theoretically analyze and compare the formation principle of the narrow-line with that of broad-line cooling, and achieve the momentum space crystal in experiment. Beyond that we present a series of numerical calculations of those important parameters which influence the distribution and size of the momentum space crystal. Correspondingly, we vary the values of these parameters in experiment to observe the momentum space crystal evolution and distribution. The experimental results are in conformity with the results of the theoretically numerical calculations. These results and analyses provide a detailed supplementary study on the formation and evolution of momentum space crystal. In addition, this work could also give a guideline on atomic manipulation by narrow-line cooling.

Keywords: momentum space crystal, narrow-line cooling, strontium

PACS: 37.10.–x, 03.65.Sq, 81.16.Ta **DOI:** 10.1088/1674-1056/28/1/013701

1. Introduction

Alkaline-earth metal atoms with spin-forbidden transitions are more convenient for laser cooling to sub-μK temperatures compared with alkaline atoms,[1,2] which make these systems extremely useful for fundamental studies such as sub-Doppler cooling,[3,4] quantum degenerate gas,[5–7] atom interferometer,[8] and precision optical frequency metrology.[9–11] The spin-forbidden transition cooling is also called narrow-line cooling according to the ratio of the transition natural width Γ and the single-photon recoil frequency shift ω_R, showing unique properties in thermal and mechanical dynamics and fundamental atomic physical phenomena.[12,13] For example, the momentum space crystal (MSC) based on alkaline-earth metal atoms was first demonstrated for ^{88}Sr narrow-line cooling.[12] After narrow-line cooling in the magneto optical trapping (MOT), the detuning frequency of the trapping laser was changed from negative to positive. In this way, the laser would accelerate atoms resulting in the arrangement of the atoms into some discrete sets in the momentum space.

These regular momentum packets are the MSC. Later, Stellmer *et al.* also observed similar phenomenon in their experiment with ^{88}Sr Bose–Einstein condensate (BEC).[14] In the spinless boson ^{88}Sr systems, since the cooling laser and the accelerating laser used in the narrow-line cooling process have the same wavelength,[15] the system is much simpler. When it comes to the fermion ^{87}Sr atom which has a non-zero nuclear magnetic moment ($I = 9/2$), the formation of MSC in ^{87}Sr atom is affected by non-zero nuclear spin and is different from ^{88}Sr. More importantly, this phenomenon occurs in the system with incoherently excited non-degenerate thermal cloud, and extends the study of the mechanical dynamics of light–atom interactions, which is worth investigation.[14,16,17] In addition, the complexity of the red MOT is much increased,[18,19] besides the trapping laser at 689 nm, another stirring laser should be employed to enlarge the number of atoms in the red MOT and to obtain a high signal–noise ratio for the detection.[20] Meanwhile, the stirring laser can be utilized as the accelerating laser.

In this paper, we report on the MSC based on the fermion ^{87}Sr atoms. We considered the influence of ^{87}Sr hyperfine structures on MSC and analyzed its formation process. Then we used numerical calculations to analyze MSC with different parameters, including the detuning frequency, the saturation factor of the laser, and the interaction time. The experimental results of our system show good agreement with the theoretical calculations. These results provide important information for the study of MSC based on alkaline-earth metal atoms. And the method to prepare the MSC could also be implemented in the research for separating the cold atoms.

*Project supported by the National Natural Science Foundation of China (Grant Nos. 11474282 and 61775220), the Key Research Project of Frontier Science of the Chinese Academy of Sciences (Grant No. QYZDB-SSW-JSC004), and the Strategic Priority Research Program of the Chinese Academy of Sciences (Grant No. XDB21030100).

†Corresponding author. E-mail: changhong@ntsc.ac.cn

© 2019 Chinese Physical Society and IOP Publishing Ltd

2. Formation and analysis of strontium momentum space crystal

In nature, three of the four strontium atom isotopes are bosons which are ^{88}Sr, ^{86}Sr, and ^{84}Sr, and ^{87}Sr is the sole fermion in the four isotopes.[21] The MSC was first discovered with boson ^{88}Sr atoms due to its simplicity.[12,14] In contrast, ^{87}Sr atoms have a nuclear spin of $I = 9/2$, leading to the hyperfine structure of both the ground and the excited states. And the excited state ^{3}P$_1$ of ^{87}Sr is split into three hyperfine states $F = 7/2$, $9/2$, and $11/2$. The transition from the ground state $(5s^2)^1S_0(F = 9/2)$ to the excited state $(5s5p)^3P_1(F = 11/2)$ is employed to trap the atoms. However, the atoms could not be trapped so steadily in the MOT[19] due to that the 12 magnetic sub-levels of the excited state $(5s5p)^3P_1(F = 11/2)$ split largely, and the atoms in some of the stretched states are expelled from the center of the trap. Therefore, a stirring light $(5s^2)^1S_0(F = 9/2)$–$(5s5p)^3P_1(F = 9/2)$ is added to solve the problem, which can stir the ground state m_F distribution of the atoms randomly and improve the cooling efficiency.[22] In this way, we can not only increase the number of cooling atoms in the red MOT, but also reduce the temperature of the atoms to a few μK.

The atoms in the red MOT are cooled close to the Doppler limit. Meanwhile, these atoms can be easily accelerated by the positive detuning frequency laser. Considering the atomic resonance $^1S_0(F = 9/2)$–$^3P_1(F = 9/2)$ frequency ω_A and the laser frequency ω_L, the scattering force can be written as

$$\boldsymbol{F}(\boldsymbol{v}) = \frac{\hbar \boldsymbol{k} \Gamma}{2}\left[\frac{s}{1+s+4\left(\Delta-\boldsymbol{k}\cdot\boldsymbol{v}\right)^2/\Gamma^2} - \frac{s}{1+s+4\left(\Delta+\boldsymbol{k}\cdot\boldsymbol{v}\right)^2/\Gamma^2}\right], \tag{1}$$

where Δ is the detuning frequency with $\Delta = 2\pi\delta = \omega_L - \omega_A$, Γ is the natural linewidth of the atomic resonance with $\Gamma = 2\pi \times 7.5$ kHz, $\boldsymbol{k}$ is the wave vector of the accelerating laser, and s is the saturation factor of the accelerating laser. According to Eq. (1), the atoms are accelerated when the detuning frequency is positive since the accelerating laser provides a positive feedback.[16,23,24] Given sufficient interaction time between atoms and lasers, the velocity of the atoms will be accelerated to the final velocity $v = \left(\Delta + \Gamma\sqrt{1+s}/2\right)k$. As seen, the final velocity is not determined by the initial value of the atoms which are cooled and the mass of the strontium, but positively correlated to the laser detuning frequency Δ and saturation factor s.

As far as the ^{87}Sr system in this article is concerned, when the magnetic field is not zero, the atoms at each magnetic sublevel m_F can absorb photons, leading to the acceleration of the atoms by the recoil momentum. And the MSC at the different magnetic sublevels will be blended.[14] In the same magnetic field, the larger Landé g-factor of the hyperfine energy level corresponds to larger Zeeman splitting. Then, the MSC formation is more complex. Because the Zeeman shift of the $^1S_0(F = 9/2)$–$^3P_1(F = 9/2)$ stirring transition with $g_F = 2/33$ is 4.5 times smaller than that of the $^1S_0(F = 9/2)$–$^3P_1(F = 11/2)$ trapping transition with $g_F = 3/11$, the stirring transition is not sensitive to the magnetic field and is suitable to use for accelerating the atoms.[14]

We quantitatively analyze the one-dimensional MSC with zero-magnetic field.[16] According to the semi-classical theory and the definition of scattering force in Eq. (1), we can obtain the equation of motion of the atom

$$\frac{\partial v}{\partial t} = \frac{\hbar k \Gamma}{2m}\left[\frac{s}{1+s+4(\Delta-kv)^2/\Gamma^2} - \frac{s}{1+s+4(\Delta+kv)^2/\Gamma^2}\right], \tag{2}$$

where m is the mass of ^{87}Sr atom. Integrating the two variables in Eq. (2), we can obtain the dependence of the interaction time t on the initial velocity v_i and the final velocity v, where v_i is the velocity corresponding to the atomic cooling and v is the velocity at which the MSC is formed,

$$t = \frac{m}{8k^2 s\Gamma^3\Delta\hbar}\left[4k^2(v^2-v_i^2)\left(k(v^2+v_i^2)+(1+s)\Gamma^2-4\Delta^2\right) + \left((1+s)\Gamma^2+4\Delta^2\right)^2(\log(v)-\log(v_i))\right]. \tag{3}$$

2.1. The evolution of the final velocity with interaction time

Figure 1 characterizes the required time for the atom to accelerate to the final velocity, which is plotted according to Eq. (3) based on the narrow-line cooling $(5s^2)^1S_0$–$(5s5p)^3P_1$ (689 nm). The blue dashed lines parallel to the X-axis in Fig. 1 indicate the interaction time $t = 20$ ms. The cross points of the blue dashed line and all the other curves represent the value

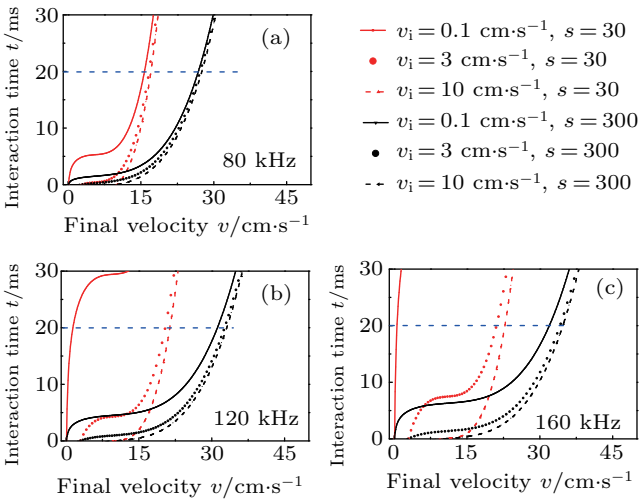


Fig. 1. Evolution of the final velocity with the interaction time based on the narrow-line cooling $(5s^2)^1S_0$–$(5s5p)^3P_1$ (689 nm) at detuning frequency (a) 80 kHz, (b) 120 kHz, and (c) 160 kHz, respectively. The blue dashed line in the figure is the interaction time $t = 20$ ms.

of the final velocity after 20 ms interaction time. In addition, because the initial atomic velocity distribution in narrow-line cooling is a normal distribution, we selected three values from the atomic velocity distribution at an average temperature of 5 μK: 0.1 cm·s^{-1}, 3 cm·s^{-1} (most probable speed), and 10 cm·s^{-1}.

Figure 1(a) shows that at $s = 30$ and $\delta = 80$ kHz, three initial atomic velocities v_i evolve to the same final velocity v of 15 cm·s^{-1}. When the detuning frequency increases, the distribution of the final velocity v changes. The final velocity is not the same for the atoms with different v_i. For example, when $s = 30$ and $\delta = 160$ kHz (Fig. 1(c)), the final velocity will evolve to 0.6 cm·s^{-1} and 21 cm·s^{-1} for different initial atomic velocities of 0.1 cm·s^{-1}, 3 cm·s^{-1}, and 10 cm·s^{-1}, respectively. In addition, at $s = 300$, v becomes to a unique value $v = 27$ cm·s^{-1} at $\delta = 80$ kHz, $v = 33$ cm·s^{-1} at $\delta = 120$ kHz, and $v = 34$ cm·s^{-1} at $\delta = 160$ kHz. As shown in Fig. 1, it is proved that the value of v increases and multiple v envelopes are not easy to achieve with the increase of the saturation factor s. In a word, it can be concluded that when the atoms are accelerated by a positive detuning frequency of the laser, the atomic velocity will evolve from the original thermodynamic distribution to a discrete momentum space envelope, and consequently form the MSC.

2.2. Numerical calculations of the MSC based on narrow-line cooling $^1S_0$–$^3P_1$

2.2.1. Formation of the MSC in the horizontal direction

Figures 2(a)–2(c) show the final velocity v versus initial velocity v_i in momentum (velocity) space with different saturation factors and detuning frequencies according to Eq. (3). The initial velocity v_i of the atom within 3 cm·s^{-1} corresponds to different final velocities in Fig. 2(a). When the saturation factor increases to 100 or even 300, v becomes a unique value regardless of v_i, as shown in Figs. 2(b) and 2(c), this is similar to the phenomenon in Fig. 1. In addition, with the increase of the detuning frequency, the final velocity increases, but the distribution of final velocity changes slightly.

Figures 2(d)–2(f) show the spatial distribution of the MSC in the horizontal direction of position space with different saturation factors and detuning frequencies. As the saturation factor increases, the number of the envelopes decreases from three to two. The influence of the saturation factor not only affects the number of envelopes, but also affects the size of the MSC. With the increase of the saturation factor, the scattering force increases, thus the interval of the envelope increases, resulting in an increase of the MSC's size. While the influence of the detuning frequency to the size of MSC is small.

In addition to the saturation factor and the detuning frequency, the interaction time t is also an important factor affecting the spatial distribution and size of the MSC. Figure 3(a) shows the distribution of final velocity v for various interaction time t with $s = 100$ and $\delta = 120$ kHz, revealing that the value of v remains almost the same. However, as shown in Fig. 3(b), the longer the interaction time, the larger the size of the MSC.

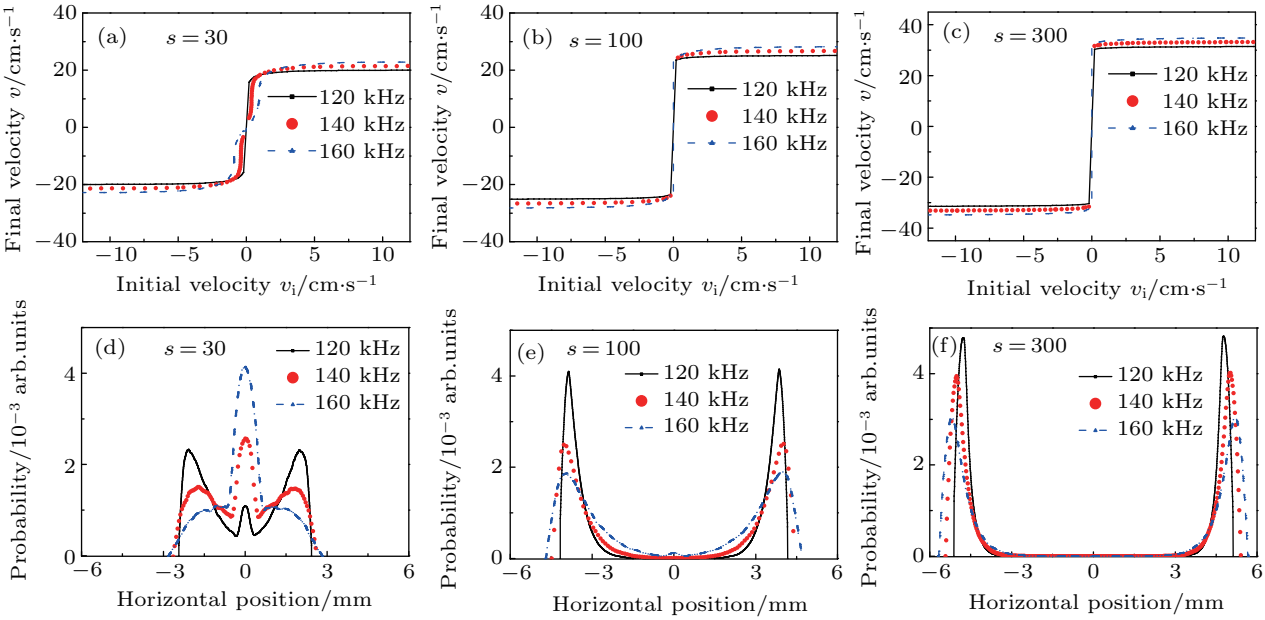


Fig. 2. Numerical calculations of the MSC based on narrow-line cooling $(5s^2)^1S_0$–$(5s5p)^3P_1$ (689 nm), showing the final velocity distribution for various initial velocities and the horizontal spatial distribution of the MSC at an interaction time of 20 ms. The distribution of final velocity versus initial velocity is shown for saturation factors of (a) $s = 30$, (b) $s = 100$, and (c) $s = 300$. Panels (d)–(f) show the corresponding spatial distributions of the MSC with those saturation factors. The black solid, red dot, and blue dash lines show data for detuning frequencies of 120 kHz, 140 kHz, and 160 kHz, respectively, at an initial atomic temperature of 5 μK.

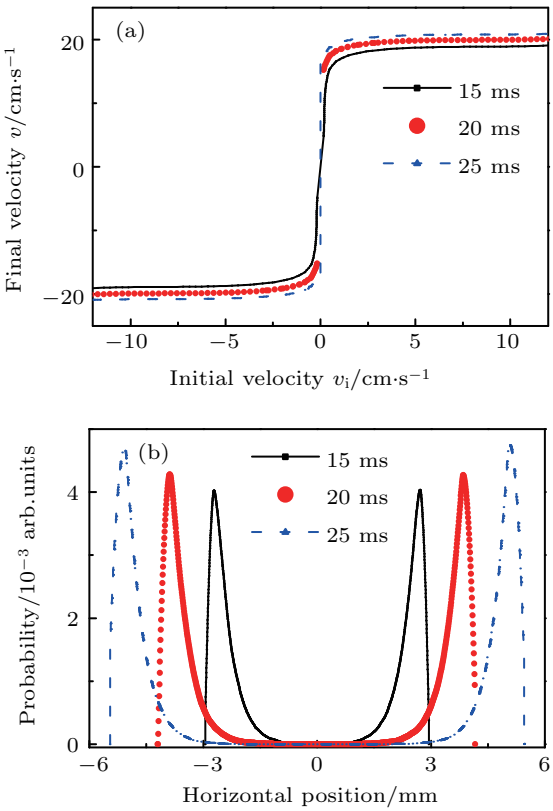


Fig. 3. The MSC with different interaction times. (a) The distribution of final velocity versus initial velocity at interaction time of 15 ms (black solid), 20 ms (red dot), and 25 ms (blue dash), with $s = 100$ and $\delta = 120$ kHz. (b) Variation in the MSC spatial distribution with interaction time of 15 ms, 20 ms, and 25 ms.

2.2.2. Formation of the MSC in the vertical direction

We analyzed the distribution of v in the momentum space before. However, the spatial distribution is the main basis for our analysis of the size and shape of the MSC, so in this paper we focus on the calculation of the spatial distribution in the vertical direction. In the vertical direction, to consider the influence of the gravity on the MSC, we added gravitational acceleration g to Eq. (2). By comparing with the calculated results of the MSC at different parameters, we summarized the evolution rules of the MSC in the vertical direction.

Figure 4(a) shows the spatial distribution of MSC in the vertical direction at different detuning frequencies. The zero point is the position of the initial cooling atom cloud, and the opposite direction of gravity is the positive direction. There are similar phenomena in Fig. 4(a) and Fig. 2: the size of the MSC changes slightly as the detuning frequency increases. However, there is some difference between Fig. 4(a) and Fig. 2: the distribution of the atomic envelope is asymmetric. Because of the gravity, the atoms at the bottom of the zero point have a larger probability of distribution than those at the top. Another feature of Fig. 4(a) is that as the detuning frequency increases, the distribution probability of the atoms at the top decreases. This behavior occurs because of the increase in the detuning frequency, which reduces the scattering force, and the accelerating laser is not sufficient to push up the atoms overcoming gravity.

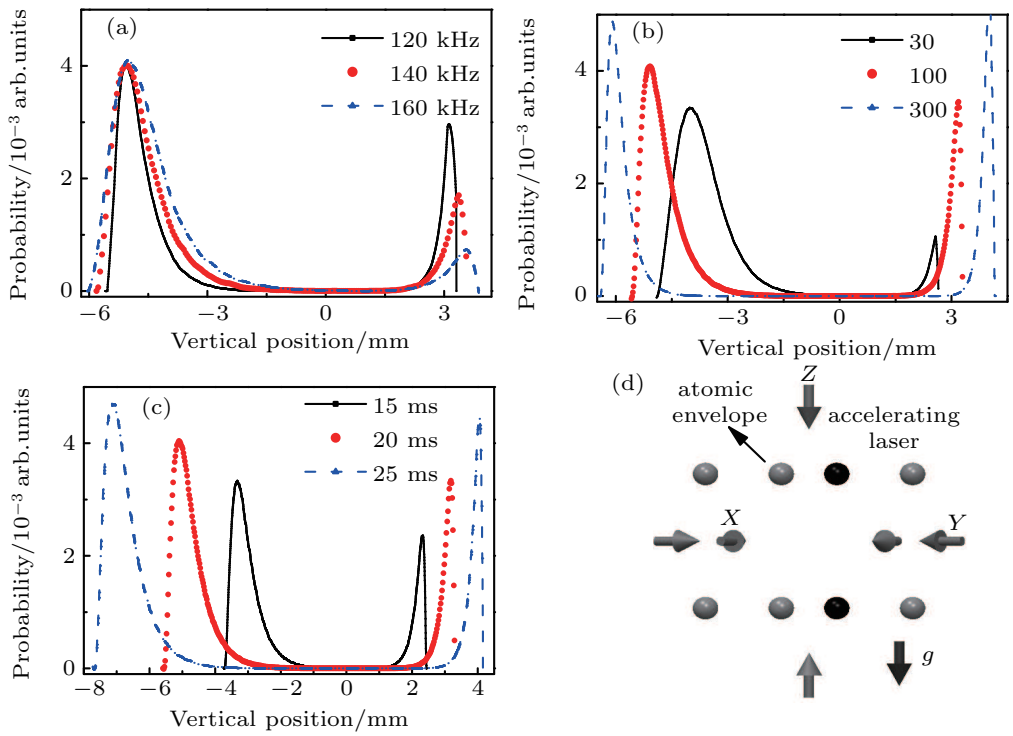


Fig. 4. Side view of the model and the MSC numerical calculations in the vertical direction. The MSC spatial distribution is shown for an initial atomic temperature of 5 μK. The spatial distributions are shown (a) at detuning frequencies of 120 kHz (black solid), 140 kHz (red dot), and 160 kHz (blue dash), for $t = 20$ ms and $s = 100$; (b) at saturation factors of $s = 30$ (black solid), $s = 100$ (red dot), and $s = 300$ (blue dash), for $t = 20$ ms and $\delta = 120$ kHz; and (c) at interaction time of $t = 15$ ms (black solid), $t = 20$ ms (red dot), $t = 25$ ms (blue dash), for $s = 100$ and $\delta = 120$ kHz. (d) Side view of the expected MSC model in the vertical direction at $s = 100$. In the figure, the solid balls are atomic envelopes, and the two black balls represent the atomic envelope which is closer to the observation window.

Figure 4(b) displays the influence of the saturation factor s on the spatial distribution of MSC. Compared with the results in the horizontal direction, the MSC in the vertical direction shows the same trend. As the saturation factor increases, the size of the MSC also increases. However, as the saturation factor increases, the distribution probability of the top atoms increases in Fig. 4(b). According to Eq. (1), as the saturation factor increases, the scattering force increases and more atoms are accelerated up. For example, at $s = 300$, the top and bottom atoms are about equal in distribution probability. Figure 4(c) shows the spatial distribution of MSC in the vertical direction at various interaction time. The evolution is similar to that in Fig. 3(b): the longer the interaction time, the larger the size of the MSC.

Based on these numerical calculations and analysis, we extend the above results to three-dimensional space. Under general experimental conditions, the atoms have only one final velocity in one-dimensional position space, and there are two discrete envelopes in our calculations. In three-dimensional space, we infer the presence of eight discrete spatial envelopes located at the eight vertices of the cube, so the image we observed should be the one shown in Fig. 4(d).

2.3. Numerical calculations of the MSC based on broad-line cooling $^1S_0$–$^1P_1$

The above numerical calculations are based on the narrow-line cooling $(5s^2)^1S_0$–$(5s5p)^3P_1$ (689 nm), which has $\Gamma/\omega_R = 1.6$. Theoretically, there is an MSC in broad-line cooling $(5s^2)^1S_0$–$(5s5p)^1P_1$ (461 nm), which has $\Gamma/\omega_R \sim 3 \times 10^4 \gg 1$. In other words, the MSC is a universal Doppler cooling phenomenon. However, the MSC is found in narrow-line cooling instead of broad-line cooling in experiment for the first time,[16] so it is necessary to distinguish the difference between them. In order to compare with narrow-line cooling, we give the following calculations about the MSC in broad-line cooling. The results show that it is more difficult to achieve MSC in broad-line cooling than in narrow-line cooling, since the sizes of the atomic cloud and the formed MSC are comparable.

Figure 5(a) shows v as a function of v_i based on the broad-line cooling at $t = 0.5$ ms, which has similar phenomena to the narrow-line cooling in Fig. 2. The spatial distribution in Fig. 5(b) is also similar to that in Fig. 2. However, the calculated results in Fig. 5 are larger. For example, at detuning frequency 50 MHz or 60 MHz, the final velocity is as high as 6000 cm·s^{-1}, about 200 times the final velocity in Fig. 2. The size of MSC in Fig. 5(b) based on broad-line cooling, which is between 10 mm and 20 mm, is double the size of the MSC in Fig. 2 based on narrow-line cooling.

Based on the above calculated results, we can easily observe the MSC in narrow-line cooling (689 nm) instead of broad-line cooling (461 nm). Firstly, in the experiment, we are limited by the field of view of the imaging system (the electron-multiplying charge-coupled device (EMCCD) has an effective imaging area of approximately 8 mm×8 mm). It is not practical to observe MSC in broad-line cooling. Besides, the size of the atomic cloud by the narrow-line cooling (689 nm) is a few millimeters, and the size of the MSC formed is about 10 mm, which is distinguishable. In contrast, the size of the atomic cloud in broad-line cooling (461 nm) is about 10 mm, which is equivalent to the size of the MSC formed. So it is not easy to distinguish each envelope of the MSC.

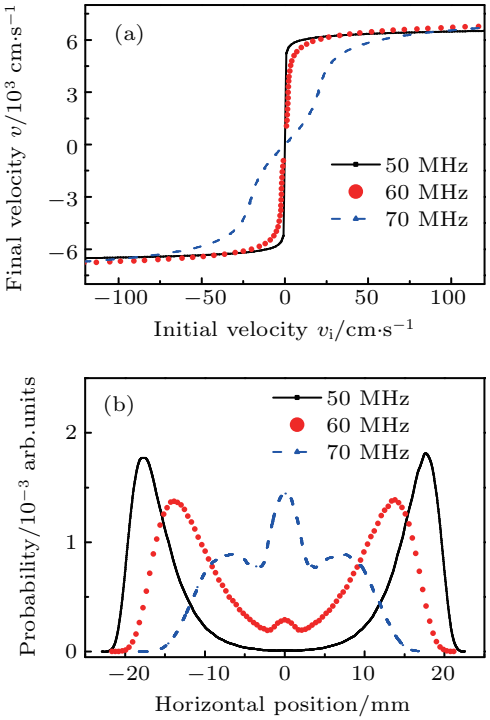


Fig. 5. Numerical calculations of the MSC based on broad-line cooling $(5s^2)^1S_0$–$(5s5p)^1P_1$ (461 nm). The calculations are in the horizontal direction at an initial atomic temperature of 3 mK and an interaction time t of 0.5 ms. (a) Final velocity versus initial velocity at detuning frequencies of 50 MHz (black solid), 60 MHz (red dot), and 70 MHz (blue dash). (b) The corresponding spatial distribution.

3. Experimental setup

Figure 6(a) shows a three-dimensional illustration of the incident laser around the MOT cavity. We used two-stage laser cooling, the primary cooling was done using the $^1S_0$–$^1P_1$ transition at 461 nm, and further cooling was done using the trapping light $^1S_0(F = 9/2)$–$^3P_1(F = 11/2)$ and the stirring light $^1S_0(F = 9/2)$–$^3P_1(F = 9/2)$ at 689 nm. The experimental optical path and device were described in detail in Ref. [9]. The counter-propagating lasers are incident along the X, Y, and Z directions. The EMCCD camera in Fig. 6 (a) is a 512 × 512-pixel EMCCD sensor with 16 μm× 16 μm wide pixels, through the lens imaging 1:1 provided an effective imaging area of approximately 8 mm×8 mm. The EMCCD observes in the X–Y plane at 30° to the X direction and

at 60° to the Y direction as shown in Fig. 6(a). The upper and lower coils are the anti-Helmholtz coils that provide the magnetic field for the MOT. The primary and secondary cooling laser beams are injected into the MOT cavity as shown in Fig. 6(a). After two-stage cooling, we measured the temperature (5 μK) of the atoms by the time-of-flight method, changed the detuning frequency of the stirring laser to be positive as the accelerating laser to form the MSC.

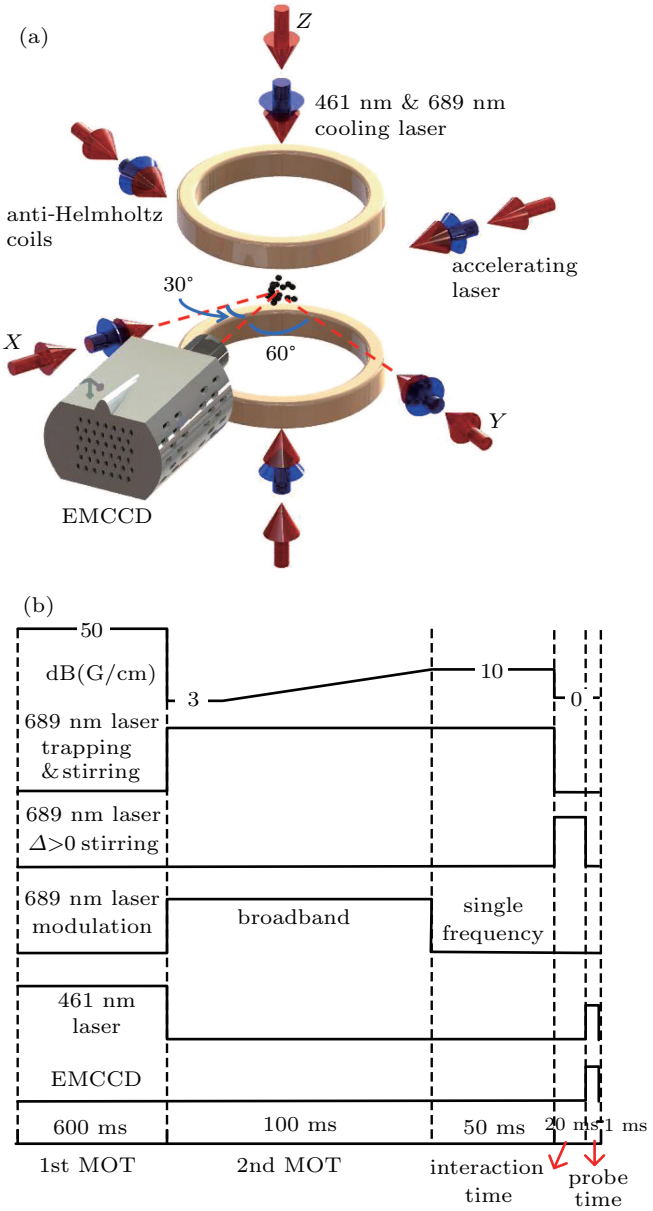


Fig. 6. Schematic of the experimental setup and timing sequence. (a) The counter-propagating incident laser from three directions. The incident optical powers of the 461 nm trapping laser, 689 nm trapping laser, and 689 nm stirring laser are 13 mW, 2 mW, and 1 mW, respectively. (b) The experimental timing sequence.

Figure 6(b) shows the timing sequence of the experiment. The secondary cooling, including broadband cooling within 100 ms and single-frequency cooling within 50 ms, follows the primary cooling. After preparing cold atoms at a micro-Kelvin temperature, we turned off the MOT magnetic field, and turned on the positive detuning stirring laser to interact with the atoms for 20 ms to form the MSC. Finally, the 461 nm laser was used as the probe laser for 1 ms, and the atomic sample was excited to emit fluorescence. The spatial distribution of the MSC atoms was photographed by EMCCD.

4. Experimental results and discussion

4.1. Influence of saturation factor and detuning frequency on the MSC

Figure 7 shows the well-defined MSCs taken by EMCCD. In this figure, the brightness is proportional to the number of atoms and the distance between the center of the atomic cloud and EMCCD. The number of atoms in each atomic envelope is proportional to the distribution probability. Figure 7 shows a consistent distribution to that in Fig. 4(d), there are eight discrete atomic envelopes. There are two atomic envelopes in the middle of the MSC that are much brighter than the other six because these envelopes are closer to the EMCCD. This result is also consistent with the result in Fig. 4(d).

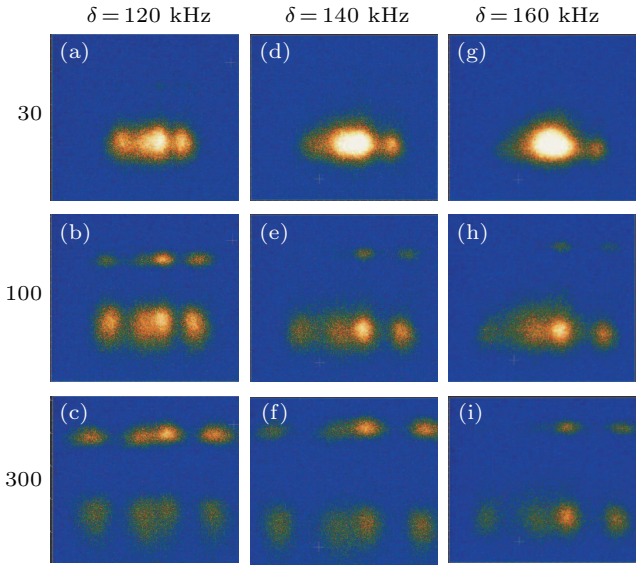


Fig. 7. MSC image at various saturation factors and detuning frequencies of the laser at $t = 20$ ms by EMCCD at an atomic temperature of 5 μK: from top to bottom, the images have saturation factors of 30, 100, and 300; from left to right, the images have detuning frequencies of 120 kHz, 140 kHz, and 160 kHz.

Comparing Figs. 7(a)–7(c), as the saturation factor increases, we find that the size of the MSC grows and the number of atoms at the top increases from zero to more, which also agrees with the calculated results in Fig. 4(b) and Fig. 2. In Figs. 7(b), 7(e), and 7(h), as the detuning frequency increases, the size of the MSC does not grow but the top atomic envelope darkens, which agrees with the numerical results of Fig. 4(a).

Comparing Fig. 2 and Fig. 4 with Figs. 7(a), 7(d), and 7(g), we did not find all envelopes in the horizontal and vertical directions. We speculate that there are two reasons. Firstly,

the MSCs formed in our experiments were not completely separated, and it is too difficult to judge whether there are more envelopes. In addition, although the rules in the calculation are consistent with the changes in the experiment, the sizes of MSC in the experiment are different from the calculated ones, so other parameters should be considered in the numerical calculations to describe the MSC more accurately.

4.2. Influence of interaction time on the MSC

Figure 8 shows the observed MSC with various interaction time between atoms and lasers. The trend of the MSC agrees with the result of the numerical calculations in Fig. 4(c). As the interaction time becomes longer, the size of the MSC becomes larger. Moreover, at $t = 15$ ms in Fig. 8(a), there is some overlap between the atomic envelopes. When the interaction time is less than 15 ms, we infer that a mixed atomic cloud will be observed.

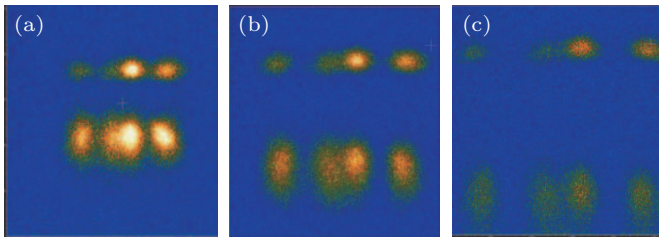


Fig. 8. MSC image at various interaction time: (a) 15 ms, (b) 20 ms, (c) 25 ms, taken by EMCCD at $\delta = 120$ kHz and $s = 100$.

Under the same experimental condition, we used the trapping laser $^1S_0(F = 9/2)$–$^3P_1(F = 11/2)$ as the accelerating laser. But we did not find similar experimental phenomena whatever parameters were used. The reason is that the trapping laser is sensitive to the magnetic field which can cause the MSCs overlap and difficult to produce a well-defined MSC.

In the experimental results of Fig. 7 and Fig. 8, we found that there are some differences between the calculation results and the experiment results such as the size of the MSC. Because in theoretical calculations, we did not consider the reduction of the total atomic number, the change of the saturation factor, and other influences. For example, the trapped cold atoms cannot completely become MSCs resulting in a decrease in the number of atoms, and the radial distribution of the laser intensity causes the saturation factor to change in the radial direction of the spot.

5. Conclusion

We found a novel semi-classical cooling process for fermion ^{87}Sr which formed the MSC in three-dimensional space by the narrow-line cooling. We chose a suitable accelerating laser for ^{87}Sr according to theoretical analysis. Then, using semi-classical theory, we evolved the formation of the MSC. In numerical calculations, we calculated the influence of different parameters on the evolution of MSC: the larger the saturation factor, the more atoms in the top envelope; the greater the detuning, the more atoms in the top envelope; the longer the interaction time, the larger the MSC. In experiment, we observed the well-defined MSC after narrow-line cooling, and verified the results in the numerical calculation. The calculated results agreed with the results of experiment. These results provide a detailed supplement to the study of MSC and a guide to the discovery of other types of MSC. In addition, this work could also give a guideline on atomic manipulation by narrow-line cooling.

References

[1] Courtillot I, Quessada A, Kovacich R P, Zondy J J, Landragin A, Clairon A and Lemonde P 2003 *Opt. Lett.* **28** 468
[2] Weiner J, Bagnato V S, Zilio S and Julienne P S 1999 *Rev. Mod. Phys.* **71** 1
[3] Xu X Y, Loftus T H, Dunn J W, Greene C H, Hall J L, Gallagher A and Ye J 2003 *Phys. Rev. Lett.* **90** 193002
[4] Maruyama R, Wynar R H, Romalis M V, Andalkar A, Swallows M D, Pearson C E and Fortson E N 2003 *Phys. Rev. A* **68** 011403
[5] Takasu Y, Maki K, Komori K, Takano T, Honda K, Kumakura M, Yabuzaki T and Takahashi Y 2003 *Phys. Rev. Lett.* **91** 040404
[6] Stellmer S, Grimm R and Schreck F 2011 *Phys. Rev. A* **84** 043611
[7] Mickelson P G, Martinez D, Escobar Y N, Yan M, DeSalvo B J and Killian T C 2010 *Phys. Rev. A* **81** 051601
[8] Ruschewitz F, Peng J, Hinderthür H, Schaffrath N and Ertmer W 1998 *Phys. Rev. Lett.* **80** 3173
[9] Wang Y B, Yin M J, Ren J, Xu Q F, Lu B Q, Han J X, Guo Y and Chang H 2018 *Chin. Phys. B* **27** 023701
[10] Strelkin S A, Galyshev A A, Berdasov O I, Gribov A Y, Sutyrin D V, Khabarova K Y, Kolachevsky N N and Slyusarev S N 2015 *Phys. Procedia* **72** 184
[11] Curtis E A, Oates C W and Hollberg L 2003 *J. Opt. Soc. Am. B* **20** 977
[12] Loftus T H, Ido T, Ludlow A D, Boyd M M and Ye J 2004 *Phys. Rev. Lett.* **93** 073003
[13] Norcia M A, Cline J R K, Bartolotta J P, Holl M J and Thompson J K 2018 *New J. Phys.* **20** 023021
[14] Stellmer S 2013 *Degenerate Quantum Gases of Strontium* (Ph. D. Dissertation) (Innsbruck: Computer Science and Physics of the University of Innsbruck)
[15] Katori H, Ido T, Isoya Y and Kuwata-Gonokami M 1999 *Phys. Rev. Lett.* **82** 1116
[16] Loftus T H, Ido T, Boyd M M, Ludlow A D and Ye J 2004 *Phys. Rev. A* **70** 063413
[17] Stellmer S, Schreck F and Killian T C 2014 *J. Opt. Soc. Am. B* **20** 1
[18] Wang Q, Lin B K, Zhao Y, Li Y, Wang S K, Wang M M, Zang E J, Li T C and Fang Z J 2011 *Chin. Phys. Lett.* **28** 033201
[19] Mukaiyama T, Katori H, Ido T, Li Y and Kuwata-Gonokami M 2003 *Phys. Rev. Lett.* **90** 113002
[20] Michael J M 2006 *Quantum Metrology and Many-Body Physics: Pushing the Frontier of the Optical Lattice Clock* (Ph. D. Dissertation) (Colorado: the University of Colorado)
[21] Berglund M and Wieser M E 2011 *Pure Appl. Chem.* **83** 397
[22] Boyd M M, Zelevinsky T, Ludlow A D, Foreman S M, Blatt S, Ido T and Ye J 2006 *Science* **314** 1430
[23] Lett P D, Phillips W D, Rolston S L, Tanner C E, Watts R N and Westbrook C I 1989 *J. Opt. Soc. Am. B* **6** 2084
[24] Phillips W D 1998 *Rev. Mod. Phys.* **70** 721
[25] Courtillot I, Quessada-Vial A, Brusch A, Kolker D, Rovera G D and Lemonde P 2005 *Eur. Phys. J. D* **33** 161